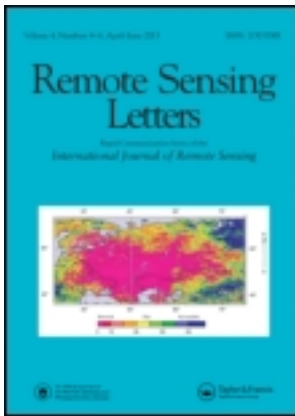


This article was downloaded by: [University Of Maryland]

On: 20 November 2013, At: 18:34

Publisher: Taylor & Francis

Informa Ltd Registered in England and Wales Registered Number: 1072954 Registered office: Mortimer House, 37-41 Mortimer Street, London W1T 3JH, UK



Remote Sensing Letters

Publication details, including instructions for authors and subscription information:

<http://www.tandfonline.com/loi/trsl20>

A decomposition-free scattering mechanism classification method for PolSAR images with Neumann's model

Xiaoguang Cheng^a, Wenli Huang^b & Jianya Gong^a

^a State Key Laboratory of Information Engineering in Surveying, Mapping and Remote Sensing, Wuhan University, Wuhan, China

^b Department of Geographical Sciences, University of Maryland, College Park, MD, USA

Published online: 20 Nov 2013.

To cite this article: Xiaoguang Cheng, Wenli Huang & Jianya Gong (2013) A decomposition-free scattering mechanism classification method for PolSAR images with Neumann's model, Remote Sensing Letters, 4:12, 1176-1184

To link to this article: <http://dx.doi.org/10.1080/2150704X.2013.858840>

PLEASE SCROLL DOWN FOR ARTICLE

Taylor & Francis makes every effort to ensure the accuracy of all the information (the "Content") contained in the publications on our platform. However, Taylor & Francis, our agents, and our licensors make no representations or warranties whatsoever as to the accuracy, completeness, or suitability for any purpose of the Content. Any opinions and views expressed in this publication are the opinions and views of the authors, and are not the views of or endorsed by Taylor & Francis. The accuracy of the Content should not be relied upon and should be independently verified with primary sources of information. Taylor and Francis shall not be liable for any losses, actions, claims, proceedings, demands, costs, expenses, damages, and other liabilities whatsoever or howsoever caused arising directly or indirectly in connection with, in relation to or arising out of the use of the Content.

This article may be used for research, teaching, and private study purposes. Any substantial or systematic reproduction, redistribution, reselling, loan, sub-licensing, systematic supply, or distribution in any form to anyone is expressly forbidden. Terms & Conditions of access and use can be found at <http://www.tandfonline.com/page/terms-and-conditions>

A decomposition-free scattering mechanism classification method for PolSAR images with Neumann's model

XIAOGUANG CHENG*[†], WENLI HUANG[‡] and JIANYA GONG[†]

[†]State Key Laboratory of Information Engineering in Surveying, Mapping and Remote Sensing, Wuhan University, Wuhan, China

[‡]Department of Geographical Sciences, University of Maryland, College Park, MD, USA

(Received 27 June 2013; accepted 17 October 2013)

This letter focuses on scattering mechanism classification of polarimetric synthetic aperture radar (PolSAR) images. Scattering mechanism classes are defined as the different combinations of dominant and secondary scattering mechanisms. By analysing the general characteristics of surface scattering, double-bounce scattering and volume scattering, we propose a maximum likelihood classifier to classify PolSAR pixels into nine classes with three PolSAR metrics. The probability density functions of various classes are obtained via extensive simulations. This method is not only a good classification method free of polarimetric decomposition but can also serve as a pre-classification step for advanced classification scheme as well. Furthermore, it is able to simplify incoherent polarimetric decomposition, so that we can employ incoherent scattering models for all components.

1. Introduction

In polarimetric synthetic aperture radar (PolSAR) remote sensing, using scattering mechanisms information for land-cover classification is a hot trend (Qi *et al.* 2012). At present, incoherent polarimetric decomposition is the main approach to obtain scattering mechanisms information about natural targets (Freeman and Durden 1998).

Most incoherent decompositions fall into two categories: eigen-decomposition-based decomposition (EDBD, (Cloude and Pottier 1997)) and scattering-model-based decomposition (SMBD). Metrics from EDBD and SMBD are fully investigated and utilized in PolSAR classification (Cloude and Pottier 1997, Lee *et al.* 2004, Qi *et al.* 2012). However, both EDBD and SMBD have their limitations. Some researchers have found that EDBD metrics only slightly improve PolSAR classification (Freitas *et al.* 2008). In SMBD, the overestimation of volume scattering often makes the decomposition result violate the non-negative eigenvalue constraint (van Zyl *et al.* 2011). The number of knowns and unknowns are usually unequal, so certain assumptions about complex scattering coefficients are required (Freeman and Durden 1998).

However, van Zyl pointed out that different mechanisms may produce the same Mueller matrix (van Zyl 1989). Therefore, getting a unique and precise

*Corresponding author. Email: shenjianzi.cheng@gmail.com

decomposition from PolSAR data is difficult. But, we can group pixels into general classes of scattering mechanisms according to the characteristics of possible mechanisms (van Zyl 1989). In addition, for PolSAR image classification, getting basic scattering mechanism information (i.e., dominant and secondary mechanism) is often enough for a simple land-cover classification and for being used as a pre-classification step for advanced classification methods. Such information is also beneficial for the simplification of incoherent decomposition. If we only include dominant and secondary scattering mechanism in decomposition, we can use incoherent models for them so the number of knowns and unknowns can be roughly the same, then we can get good solution while preserving most polarimetric information.

The unsupervised method proposed by van Zyl (van Zyl 1989) can identify dominant scattering mechanism. But in this method, sufficient processing is not done to let Mueller matrix satisfy the assumption of azimuthal symmetry. This method varies orientation angles of the transmitted wave and computes the corresponding scattered wave, so it is time-consuming. In its experiment, certain number of pixels could not be classified. Another unsupervised scattering mechanism classification method is H/α method, proposed by Cloude and Pottier (1997) on the basis of EDBD.

With three metrics obtained from observed coherency matrix, this letter raises a supervised maximum likelihood classifier to classify pixels into nine classes that are combinations of dominant and secondary scattering mechanisms. Probability density functions (PDF) of all classes are acquired by simulations. Experimental results show that the proposed method is at least as good as H/α method and even better in some cases.

2. Definition of dominant and secondary scattering mechanisms

In SMBD, every embedded scattering mechanism is called a ‘component’. Surface scattering, double-bounce scattering, volume scattering and helix scattering are the most widely used canonical scattering mechanisms. With them, SMBD can be expressed as

$$\langle \mathbf{T} \rangle = P_h \mathbf{T}_h + P_s \mathbf{T}_s + P_d \mathbf{T}_d + P_v \mathbf{T}_v \quad (1)$$

where \mathbf{T} is observed coherency matrix, $\langle \rangle$ stands for ensemble average processing, \mathbf{T}_h , \mathbf{T}_s , \mathbf{T}_d and \mathbf{T}_v are trace-normalized models of helix scattering, surface scattering, double-bounce and volume scattering, respectively. P_h , P_s , P_d and P_v are the corresponding component powers. Given the fact that in real data, helix scattering power is quite small when compared to total power (Yamaguchi *et al.* 2005), only the cases of other three mechanisms are discussed in this letter. By subtracting helix scattering from \mathbf{T} , the remainder matrix \mathbf{T}_{noh} only contains surface scattering, double-bounce and/or volume scattering. Here, if the power of one component is larger than $(P_s + P_d + P_v)/2$, then we define this mechanism as dominant; else, if the power of one component is smaller than dominant mechanism but larger than other components, then it is secondary mechanism. In the next section, T_{ij} denotes the element in row i and column j of T .

3. Characteristics of three canonical scattering mechanisms

3.1 $\langle T_{11} \rangle$

Assume the scattering matrix of a scatterer with orientation angle $\theta = 0$ is

$$\mathbf{S} = \begin{bmatrix} S_{\text{HH}} & 0 \\ 0 & S_{\text{VV}} \end{bmatrix} \quad (2)$$

where S_{HH} and S_{VV} are complex scattering coefficients, the subscript HH stands for horizontal transmitting and horizontal receiving and the subscript VV stands for vertical transmitting and vertical receiving. Equation (2) can well describe the elemental scatterers of all the three mechanisms (Freeman and Durden 1998). Following the surface scattering model in Freeman and Durden (1998) and ground scattering model in Freeman (2007), we assume $S_{\text{HH}} = 1$, $S_{\text{VV}} = b_1 + b_2i$ and b_1 and b_2 are real and imaginary part of S_{VV} , respectively, then

$$\begin{aligned} T_{11} &= \frac{(1 + b_1)^2 + b_2^2}{2(1 + b_1^2 + b_2^2)} \\ T_{22} + T_{33} &= \frac{(1 - b_1)^2 + b_2^2}{2(1 + b_1^2 + b_2^2)} \end{aligned} \quad (3)$$

For double-bounce, $b_1 < 0$; for volume scattering, $b_1 = b_2 = 0$ (if horizontal dipole is elemental scatterer); for surface scattering, $b_1 > 0$ (Freeman and Durden 1998). As a result, in double-bounce model, $T_{11} < 0.5 < T_{22} + T_{33}$; in volume scattering model, $T_{11} = 0.5 = T_{22} + T_{33}$; in surface scattering model, $T_{11} > 0.5 > T_{22} + T_{33}$. In view that \mathbf{T} is often a mixture of several mechanisms, we postulate that \mathbf{T}_{noh} contains two mechanisms: one is volume scattering with power P_v and the other is either surface scattering or double-bounce with power $1 - P_v$. Similar assumption was made in Freeman (2007) for forest area, considering that surface scattering model and double-bounce model are mathematically equivalent. Then in \mathbf{T}_{noh} ,

$$\langle T_{11} \rangle - 0.5 = \frac{b_1}{1 + b_1^2 + b_2^2} (1 - P_v) \quad (4)$$

From equation (4), we can know that non-zero surface scattering leads to $T_{11} > 0.5$ and non-zero double-bounce leads to $T_{11} < 0.5$. The larger the P_v , the closer is $T_{11} - 0.5$ to 0; when b_1 is a fixed positive number, the larger the P_s , the larger is $T_{11} - 0.5$; when b_1 is a fixed negative number, the larger the P_d , the smaller is $T_{11} - 0.5$.

3.2 $\langle T_{33} \rangle$

Incoherent scattering model is determined by both elemental scatterer and PDF of orientation angle $p(\theta)$. With unimodal circular normal von Mises distribution, a volume scattering model \mathbf{T}_{Neum} (see equation (5)) was raised in Neumann *et al.* (2009). As a generic incoherent scattering model, \mathbf{T}_{Neum} also applies to surface scattering and double-bounce scattering.

$$\mathbf{T}_{\text{Neum}} = \frac{1}{L + N} \begin{bmatrix} L & g_c(\tau)M & 0 \\ g_c(\tau)M^* & (1 + g(\tau))N/2 & 0 \\ 0 & 0 & (1 - g(\tau))N/2 \end{bmatrix} \tag{5}$$

with $L = |S_{\text{HH}} + S_{\text{VV}}|^2$ $M = (S_{\text{HH}} - S_{\text{VV}})^*(S_{\text{HH}} + S_{\text{VV}})$ $N = |S_{\text{HH}} - S_{\text{VV}}|^2$
 $\tau = I_0(k)e^{-k}$ $g(\tau) = I_2(k)/I_0(k)$ $g_c(\tau) = I_1(k)/I_0(k)$

Here, * is the sign of complex conjugate operator; τ , as the randomness of $p(\theta)$, is in the range of $[0, 1]$; k is the concentration degree of $p(\theta)$; $I_n(k)$ is modified Bessel function of order n and parameter k . In equation (5), T_{33} is expressed as

$$T_{33} = \frac{1 - T_{11}}{2}(1 - g(\tau)) \tag{6}$$

where $g(\tau)$ is a monotonic decreasing function in $[0, 1]$ with $g(0) = 1$ and $g(1) = 0$. Combining equation (3) with (6), we can know that, for the same τ , double-bounce gives the largest T_{33} , volume scattering gives the second largest value and surface scattering gives the smallest value. Figure 1(a) is an illustration. As shown in Neumann *et al.* (2009), in real conditions, surface scattering usually has small τ , yielding small T_{33} . On the contrary, in forest, τ lies in $[0.6, 0.9]$; consequently, in volume scattering model, T_{33} varies between 0.23 and 0.25. As to double-bounce scattering, τ is also often low, but as depicted in figure 1(a), T_{33} can be over 0.23 even when τ is below 0.3. Hence, the T_{33} range of double-bounce and volume scattering may overlap.

3.3 $|\rho_{12}|$

In \mathbf{T}_{Neum} , $|\rho_{12}|$, the modulus of the correlation coefficient between T_{11} and T_{22} , is

$$|\rho_{12}| = \sqrt{2}g_c(\tau) / \sqrt{1 + g(\tau)} \tag{7}$$

Clearly, $|\rho_{12}|$ depends only on τ or corresponding k . Figure 1(b) shows that $|\rho_{12}|$ is a monotonic decreasing function of τ in $[0, 1]$. When $\tau < 0.2$, $|\rho_{12}|$ is pretty close to 1.

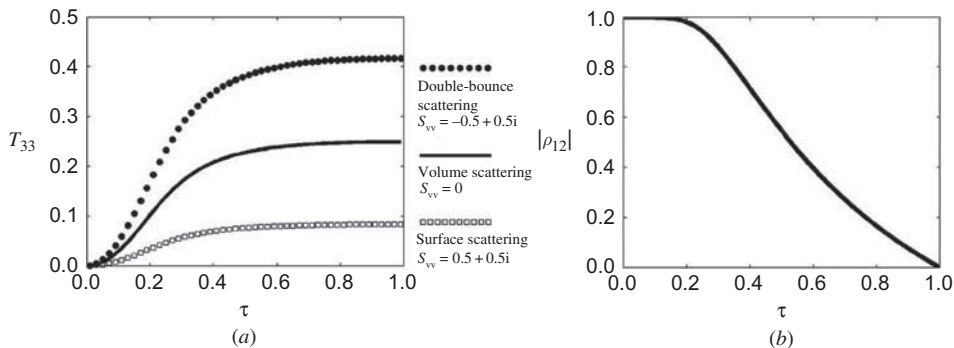


Figure 1. Neumann's model. (a) T_{33} vs. τ ; (b) $|\rho_{12}|$ vs. τ .

As pointed out in the previous section, volume scattering has large τ , yielding $|\rho_{12}|$ much smaller than that of surface scattering and double-bounce scattering.

4. Method

4.1 Metrics computation

The flow chart of proposed method is given in figure 2. \mathbf{T}_{noh} is calculated using

$$\langle \mathbf{T}_{\text{noh}} \rangle = \langle \mathbf{T} \rangle - P_h \mathbf{T}_h \tag{8}$$

\mathbf{T}_h and the method to compute P_h can be found in Yamaguchi *et al.* (2005). \mathbf{T}_{Neum} explicitly assumes the symmetric centre of $p(\theta)$ is 0. To let \mathbf{T}_{noh} roughly satisfy this assumption, perform orientation angle compensation (Lee and Ainsworth 2011) to \mathbf{T}_{noh} and get the compensated matrix $\mathbf{T}_{\text{noh_OAC}}$. We denote the diagonal elements of span-normalized $\mathbf{T}_{\text{noh_OAC}}$ as T_{11} , T_{22} and T_{33} . $|\rho_{12}|$ is computed by

$$|\rho_{12}| = |\langle T_{12} \rangle| / \sqrt{\langle T_{11} \rangle \langle T_{22} \rangle} \tag{9}$$

4.2 Simulation

T_{11} , T_{33} and $|\rho_{12}|$ form a 3D space, named $T_{11} - T_{33} - |\rho_{12}|$. Every \mathbf{T} has a mapping point in that space. For real \mathbf{T} , we cannot easily know their real dominant and secondary scattering mechanisms. To perform a supervised classification, extensive simulations of \mathbf{T} are executed to get the PDF of different classes in that space. The simulation framework is established with the core idea presented in equation (1), but helix scattering is not embedded. All three embedded mechanisms were modelled by \mathbf{T}_{Neum} . For surface scattering, $S_{\text{HH}} = 1$; for double-bounce, $S_{\text{VV}} = 1$; for volume scattering $S_{\text{HH}} = 1$ and $S_{\text{VV}} = 0$. The ranges of other parameters are given in table 1. Finally, up to 300,000 random samples were generated.

4.3 Voxel and pixel classification

In this letter, scattering mechanism classes come from different combinations of dominant and secondary scattering mechanisms. The classes of simulated \mathbf{T} are determined according to the definition in table 2 and simulation parameters. For

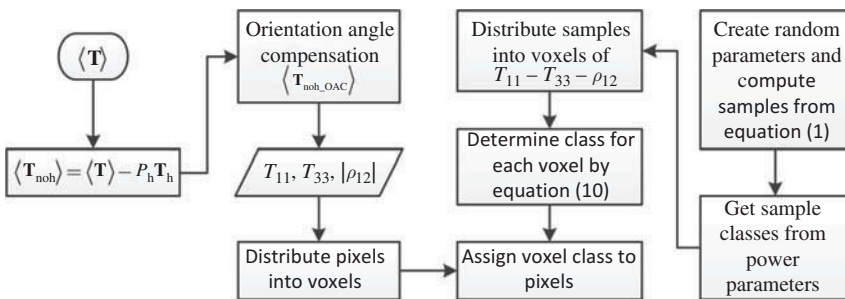


Figure 2. Flow chart of proposed method.

Table 1. The range of random parameters of different components in simulation.

| Volume | Surface scattering | | | Double-bounce scattering | | |
|------------|--------------------|------------|---------------------|--------------------------|------------|---------------------|
| τ | τ | $ S_{VV} $ | $\text{Re}(S_{VV})$ | τ | $ S_{HH} $ | $\text{Re}(S_{HH})$ |
| [0.6, 1.0] | [0.06, 0.3] | [0.3, 1.7] | [0.2, $ S_{VV} $] | [0.06, 0.3] | [0.3, 1.7] | $[- S_{HH} , -0.2]$ |

$\text{Re}(x)$ is the function to the real part of a complex number x .

Table 2. Class definitions.

| Class | 1 | 2 | 3 | 4 | 5 | 6 | 7 | 8 | 9 |
|---------------------|------|------|-----|------|------|------|------|------|------|
| Dominant mechanism | VolS | SurS | DbS | SurS | DbS | VolS | VolS | SurS | DbS |
| Secondary mechanism | - | - | - | VolS | VolS | SurS | DbS | DbS | SurS |

VolS: volume scattering; SurS: surface scattering; Dbs: double-bounce; -: unavailable.

classes 1–3, only dominant scattering mechanism is identified. Class 1, $0.49 \leq T_{11} \leq 0.51$, $0.23 \leq T_{33} \leq 0.25$; class 2, $T_{11} > 0.73$; class 3, $T_{11} < 0.27$.

The whole $T_{11} - T_{33} - |\rho_{12}|$ space is equally divided into $50 \times 50 \times 50$ voxels. All simulated \mathbf{T} are distributed into corresponding voxels. Postulate in a nonempty voxel, the number of pixels from class i is N_i , $i \in \{1, 2, \dots, 9\}$, if

$$p_n = \max(p_1, p_2, \dots, p_9) \quad \text{with} \quad p_i = \frac{N_i}{\sum_{j=1}^9 N_j}, \quad i \in \{1, 2, \dots, 9\}, \quad (10)$$

then class n is assigned to that voxel. Evidently, this is a maximum likelihood classifier. However, if p_n is not much larger than the second largest one of $\{p_1, \dots, p_9\}$, say, p_m , then there are great uncertainties concerning which class this voxel belongs to. As a result, such voxels are unclassified. Our criterion of unclassified pixel is $p_n - p_m < 0.4$. Finally, pixels are assigned the class of voxels where they locate.

Although above method is supervised, we can roughly estimate class boundaries. The boundaries for classes 1–3 are clearly provided. Next, we will analyse other classes. Observations from real data reveal that when T_{33} is lower than a small value, like 0.1, volume scattering is not dominant or secondary. Instead, surface scattering is dominant and double-bounce is secondary if $T_{11} > 0.50$ and vice versa. Section 3.1 shows that if T_{11} is close to 0.50, i.e., $|T_{11} - 0.50| < 0.05$ and $T_{33} > 0.20$, this pixel is still dominated by volume scattering. In case $T_{11} > 0.50$, surface scattering is secondary; otherwise, double-bounce is secondary. For other unclassified pixels, we adopt the postulate of pixels containing volume scattering and one ground scattering, as in section 3.1. As cited in section 3.2, τ of forest is mainly in $[0.60, 0.90]$ with corresponding $|\rho_{12}|$ in $[0.08, 0.40]$. Hence, if $|\rho_{12}| < 0.40$, the dominant mechanism is volume scattering, the secondary mechanism is surface scattering if $T_{11} > 0.50$ and double-bounce if $T_{11} < 0.50$; otherwise, the secondary mechanism is volume scattering, the dominant mechanism is surface scattering if $T_{11} > 0.50$ and double-bounce if $T_{11} < 0.50$.

5. Experiment

5.1 Verification using simulated data

To quantitatively assess the performance of our method, 3000 random samples were generated using the framework in section 4.2. Among all samples, 1466 were classified with confusion matrix given in table 3. For the remaining unclassified samples, dominant scattering mechanisms were successfully identified for 95.99% of them.

5.2 Verification using UAVSAR data

Uninhabited aerial vehicle synthetic aperture radar (UAVSAR) is an L-band airborne SAR sensor (Jet Propulsion Laboratory 2007). Our method was tested on UAVSAR data collected near Howland forest, Maine, USA, on 5 August 2009. The site consists of forests, bare land, rivers, wetlands, roads, buildings, etc. The resolution of ground range image is 5 m, and ensemble averaging is implemented in 7 pixel \times 7 pixel window.

In classification result, unclassified pixels account for 8.1% of the whole pixels. By dilating the classified image with an empirical 5 pixel \times 5 pixel window so that unclassified pixels can be assigned the classes of their surroundings, the proportion of unclassified pixels significantly dropped to 0.4%.

The results of proposed method and *H/a* method for one part of the study site are given in figure 3. Visually, in spite of large number of land-cover types, the majority of large terrain features are successfully identified by our method and *H/a* method. Most of the dense natural forests located in the left and upper part of images were assigned class 1 by *H/a* method, which only means highly random volume scattering. But our results further indicate that double-bounce is the secondary mechanism, which is consistent with the observation in Freeman (2007). In contrast, the sparse forests that are situated in the upper right corner are mostly class 6, which means surface scattering is secondary. It is in agreement with van Zyl's point of view (van Zyl 1989). However, *H/a* method still classified them as class 5 that only identifies vegetation scattering with moderate correlation of scatterer orientations. For the

Table 3. Confusion matrix of classification result. The overall accuracy is 96% and kappa coefficient is 0.947.

| Reference class | Classified class | | | | | | | | | Total | Producer's accuracy (%) |
|---------------------|------------------|-----|-----|----|----|-----|-----|----|----|-------|-------------------------|
| | 1 | 2 | 3 | 4 | 5 | 6 | 7 | 8 | 9 | | |
| 1 | 144 | 0 | 0 | 0 | 0 | 0 | 0 | 0 | 0 | 144 | 100 |
| 2 | 0 | 373 | 0 | 0 | 0 | 0 | 0 | 0 | 0 | 373 | 100 |
| 3 | 0 | 0 | 406 | 0 | 0 | 0 | 0 | 0 | 0 | 406 | 100 |
| 4 | 0 | 0 | 0 | 28 | 0 | 0 | 0 | 5 | 0 | 33 | 85 |
| 5 | 0 | 0 | 0 | 0 | 31 | 0 | 0 | 0 | 6 | 37 | 84 |
| 6 | 0 | 0 | 0 | 2 | 0 | 201 | 0 | 1 | 0 | 204 | 99 |
| 7 | 0 | 0 | 0 | 0 | 7 | 3 | 109 | 0 | 2 | 121 | 90 |
| 8 | 0 | 0 | 0 | 7 | 0 | 0 | 0 | 67 | 6 | 80 | 84 |
| 9 | 0 | 0 | 0 | 0 | 19 | 0 | 2 | 4 | 43 | 68 | 63 |
| Total | 144 | 373 | 406 | 37 | 57 | 204 | 111 | 77 | 57 | 1466 | |
| User's accuracy (%) | 100 | 100 | 100 | 76 | 54 | 99 | 98 | 87 | 75 | | |

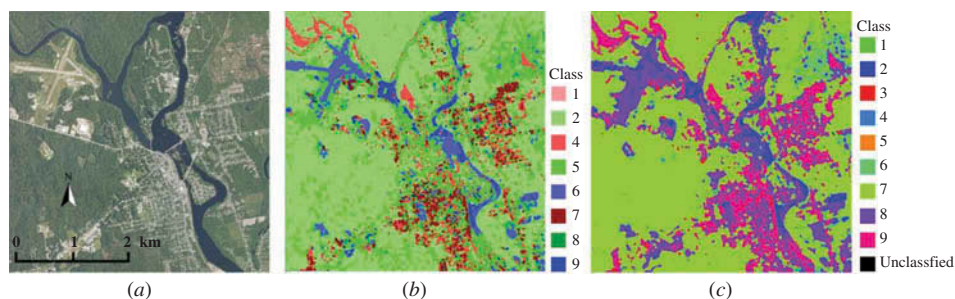


Figure 3. (a) Natural colour orthophoto; (b) Result by H/α method; (c) Result by proposed method (see table 2 for class definitions). The coordinate of upper left corner is 44.961° N, 68.683° W.

land-cover types characterized by surface scattering, like the airport and river surfaces, more pixels are identified by our method as surface-scattering dominant. In the south grassland surrounding the airport runway and the river surface near upper island, H/α method gives more class 5 pixels. As for the two large urban areas, most buildings are oriented parallel to SAR azimuth direction; so, they mainly exhibit classes 8 and 9 in our results. A few pixels near building walls exhibit class 3. At the same time, in the result by H/α method, certain number of urban pixels is considered to be dominated by volume scattering. In the southeast river surface, both methods cannot identify all pixels as surface-scattering dominant. Lastly, it seems that the result by our method shows less noise than that by H/α method, especially in forested areas.

6. Conclusion

The experiment reveals that the overall performance of our method is at least comparable to H/α method. Although the proposed method belongs to supervised classification, once the PDF of various classes and voxel classification map are obtained via extensive simulations, they can be used to many general conditions. From this perspective, it is much faster than van Zyl's method.

In some areas where surface scattering is dominant and volume scattering is secondary, the proposed method may identify double-bounce scattering as secondary (see table 3). Such areas typically have low backscatter, but areas with surface scattering as dominant mechanism and double-bounce as secondary mechanism, like urban areas, generally show strong backscatter, so the span of \mathbf{T} may be used to differentiate these two cases. Another deficiency of this method is that during simulation, the priori probabilities of various classes, which are circumstance specific, are not fully taken into consideration. In future, we may develop empirical methods to determine such priori probabilities. Lastly, the effectiveness of this method for areas without dominant scattering mechanism needs further investigation.

Acknowledgements

The authors thank anonymous reviewers for reviewing this letter.

Funding

This work was supported by National Key Fundamental Research Plan of China (973) [No. 2012CB719906].

References

- CLOUDE, S.R. and POTTIER, E., 1997, An entropy based classification scheme for land applications of polarimetric SAR. *IEEE Transactions on Geoscience and Remote Sensing*, **35**, pp. 68–78.
- FREEMAN, A., 2007, Fitting a two-component scattering model to polarimetric SAR data from forests. *IEEE Transactions on Geoscience and Remote Sensing*, **45**, pp. 2583–2592.
- FREEMAN, A. and DURDEN, S.L., 1998, A three-component scattering model for polarimetric SAR data. *IEEE Transactions on Geoscience and Remote Sensing*, **36**, pp. 963–973.
- FREITAS, C., SOLER, L., SANT'ANNA, S.J.S., DUTRA, L.V., DOS SANTOS, J.R., MURA, J.C. and CORREIA, A.H., 2008, Land use and land cover mapping in the Brazilian Amazon using polarimetric airborne P-band SAR data. *IEEE Transactions on Geoscience and Remote Sensing*, **46**, pp. 2956–2970.
- JET PROPULSION LABORATORY, NASA, 2007, *UAVSAR – Home*. Available online at: <http://uavsar.jpl.nasa.gov/instrument.html> (accessed 4 September 2013).
- LEE, J.-S. and AINSWORTH, T.L., 2011, The effect of orientation angle compensation on coherency matrix and polarimetric target decompositions. *IEEE Transactions on Geoscience and Remote Sensing*, **49**, pp. 53–64.
- LEE, J.-S., GRUNES, M.R., POTTIER, E. and FERRO-FAMIL, L., 2004, Unsupervised terrain classification preserving polarimetric scattering characteristics. *IEEE Transactions on Geoscience and Remote Sensing*, **42**, pp. 722–731.
- NEUMANN, M., FERRO-FAMIL, L. and POTTIER, E., 2009, A general model based polarimetric decomposition scheme for vegetated areas. In *The 4th International Workshop on Science and Applications of SAR Polarimetry and Polarimetric Interferometry (POLINSAR)*, ESRIN, 26–30 January, Frascati, Italy.
- QI, Z., GAR-ON YEH, A., LI, X. and LIN, Z., 2012, A novel algorithm for land use and land cover classification using RADARSAT-2 polarimetric SAR data. *Remote Sensing of Environment*, **118**, pp. 21–39.
- VAN ZYL, J.J., 1989, Unsupervised classification of scattering behavior using radar polarimetry data. *IEEE Transactions on Geoscience and Remote Sensing*, **27**, pp. 36–45.
- VAN ZYL, J.J., ARII, M. and KIM, Y., 2011, Model-based decomposition of polarimetric SAR covariance matrices constrained for nonnegative eigen-values. *IEEE Transactions on Geoscience and Remote Sensing*, **49**, pp. 3452–3459.
- YAMAGUCHI, Y., MORIYAMA, T., ISHIDO, M. and YAMADA, H., 2005, Four-component scattering model for polarimetric SAR image decomposition. *IEEE Transactions on Geoscience and Remote Sensing*, **43**, pp. 1699–1706.